Peierls potential and kink-pair mechanism in high-pressure $MgSiO_3$ perovskite: An atomic scale study

A. Kraych,[1] Ph. Carrez,[1,*] P. Hirel,[1] E. Clouet,[2] and P. Cordier[1]

[1]*Unité Matériaux Et Transformations, Bât. C6, Univ. Lille 1, 59655 Villeneuve d'Ascq, France*

[2]*CEA, DEN, Service de Recherches de Métallurgie Physique, UPSay, 91191 Gif-sur-Yvette, France*

(Received 16 July 2015; revised manuscript received 13 October 2015; published 19 January 2016)

The motion of [100](010) screw dislocations via a kink-pair mechanism is investigated in high-pressure $MgSiO_3$ perovskite by means of atomistic calculations and an elastic interaction model for kink nucleation. Atomistic calculations based on the nudged elastic band method provide the Peierls potential, which is shown to be dynamically asymmetric and stress dependent. The elastic interaction model adjusted to match kink width computed atomistically, is used to evaluate the critical nucleation enthalpy. We demonstrate that the kink-pair mechanism in $MgSiO_3$ perovskite is controlled by the nucleation of kinks along the [100] screw dislocation.

DOI: 10.1103/PhysRevB.93.014103

I. INTRODUCTION

Convective flow in the deep Earth is responsible for heat transport toward the surface and controls the global dynamics of our planet. The lower mantle, which extends between 670 and 2900 km depths is the major component of the Earth's interiors and its dynamics is therefore of primary importance. The (Al,Fe)-bearing magnesium silicate perovskite called bridgmanite is nowadays considered as the dominant phase of the mantle [1,2]. Convective flow and seismic properties in the deep mantle are thus strongly linked to the physical properties of bridgmanite under very high-pressure conditions (30–120 GPa). With the recent progress in high-pressure techniques, deformation experiments of magnesium silicate perovskite (Mg-Pv) have been successfully undertaken in lower mantle pressure and temperature conditions [3–7]. At conditions of the uppermost lower mantle ($P = 30$ GPa, close to 670 km depth), some of these studies highlighted the presence of dislocations and the development of crystal preferred orientations in the deformed samples [6,7]. A better understanding of the deformation mechanism of Mg-Pv at pressure and temperature conditions of the Earth's mantle remains, however, mandatory to evaluate the role of plastic deformation in the development of convective flow.

One of the most efficient mechanisms to produce plastic shear in crystalline materials is the motion of dislocations. In order to move, a dislocation has to overcome the intrinsic resistance of the lattice. Since the seminal work of Peierls and Nabarro [8,9], the lattice friction due to the crystalline structure is described either with the Peierls potential or through the Peierls stress. The motion of a dislocation over the Peierls potential is assisted by the conjugate effect of stress and thermal activation. During this process, the dislocation does not move as a straight line but through the nucleation and propagation of kink pairs. A small segment of dislocation line bulges over the Peierls potential. The further migration of the kinks is then responsible for the glide of the whole dislocation line [10]. Several models have been proposed [11,12], including the line tension model [11,13–15] based on line tension approximation, the kink-kink interaction model [16], or more recently an elastic interaction model [17,18]. The basic problem is to compute the enthalpy ΔH_k that has to be supplied by thermal activation to enhance the formation of a kink pair under a given stress. ΔH_k consists of three contributions: a positive increase of elastic energy of the dislocation line ΔE_{elas}, a positive increase of Peierls energy ΔW_P coming from the lying of a part of the line on the Peierls potential, and finally a negative contribution resulting from the work W_τ done by the applied stress τ. All models are thus based on the following Eq. (1) and only differ by the treatment of the change in elastic energy ΔE_{elas} [12].

$$\Delta H_k = \Delta E_{\text{elas}} + \Delta W_P - W_\tau. \tag{1}$$

The theoretical description of dislocation motion involving the kink-pair mechanism has been successfully applied to the understanding of elemental deformation processes [19] in several materials, including body-centered-cubic (bcc) metals [20–26] or covalent materials like silicon [27,28]. In those materials, the lattice resistance arises from either the particular structure of the dislocation core or from the covalent nature of bonds [29]. In contrast to metals or semiconductors, ceramics or minerals still suffer from a lack of theoretical effort to understand their plastic behavior [30–32].

Mg-Pv is a silicate with a complex crystal chemistry, that is stable only at high confining pressure. Both aspects might directly influence the Peierls potential and the energetics of the kink-pair mechanism. Following recent experimental [6] and numerical studies [33,34], we focus in this work on the properties of screw dislocation of Burgers vector [100] gliding in (010) of the orthorhombic P*bnm* perovskite structure. According to Eq. (1), the kink-pair mechanism depends on the Peierls potential. Therefore, we begin with the determination of the Peierls potential using atomistic calculations and nudged elastic band (NEB) method [35]. Then, in conjunction with atomistic calculations of the shape and enthalpy H_k of an isolated kink, we rely on an elastic interaction model [18] to

*Corresponding author: philippe.carrez@univ-lille1.fr

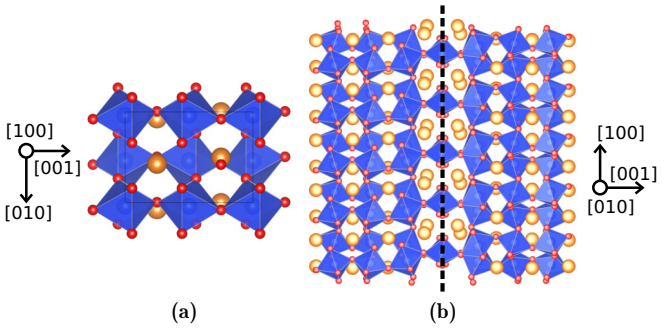

FIG. 1. (a) Mg-Pv crystal lattice viewed along [100] (Mg ions appear in yellow, Si in blue, and O in red). (b) [100] screw dislocation viewed in its (010) glide plane. The dotted line represents the dislocation line.

compute the evolution as a function of stress of the critical kink-pair nucleation enthalpy ΔH_k^*.

II. METHODS AND MODELS

In this study, we focus on the pure magnesium-rich end member (of composition $MgSiO_3$) of bridgmanite, hereinafter referred to as Mg-Pv. It exhibits an orthorhombic structure that differs slightly from the ideal cubic perovskite [36]. The arrangement of SiO_6 octahedra in the unit cell is shown in Fig. 1(a). Within the P*bnm* space group, lattice parameters of Mg-Pv at 30 GPa are $a_{[100]} = 4.6481$ Å, $b_{[010]} = 4.7615$ Å, and $c_{[001]} = 6.7178$ Å. Throughout this study, atomistic simulations are performed with the LAMMPS molecular dynamic package [37]. Interactions between ions are described with a rigid-ion pairwise potential, using the parametrization proposed by Oganov and co-workers [38]. This potential was initially evaluated for the quality of its representation of structural, elastic, and thermal properties of $MgSiO_3$, including its accuracy to reproduce the equation of state of Mg-Pv [38,39]. More recently, it has also been successfully validated to model generalized stacking fault energies [40], and dislocation core structures [34] in Mg-Pv. Here, we focus on the screw dislocation of Burgers vector [100]. The atomic core structure of this dislocation has been extensively described in a previous work [34]; we briefly recall that the main spreading of the core is found in (010) with a stable configuration centered on a corner of two joined octahedron, as illustrated in Fig. 1(b). In the following, we use b to refer to the length of the Burgers vector 4.6481 Å, and a' corresponds to the periodicity of the Peierls potential in (010), i.e., the shortest lattice repeat along [001] $a' = 6.7178$ Å.

In order to account for the pressure on the system and the use of charged potentials, all atomistic calculations rely on fully periodic system to avoid spurious effects of free surfaces. Dipole configurations of two opposite dislocations are therefore used as described in Fig. 2. For the evaluation of the Peierls potential, thanks to the periodicity along the screw line, the system can be considered as two-dimensional (2D), with the third dimension restricted to one Burgers vector length along the line direction. However, a full three-dimensional (3D) system is used to compute the kinked dislocation line as

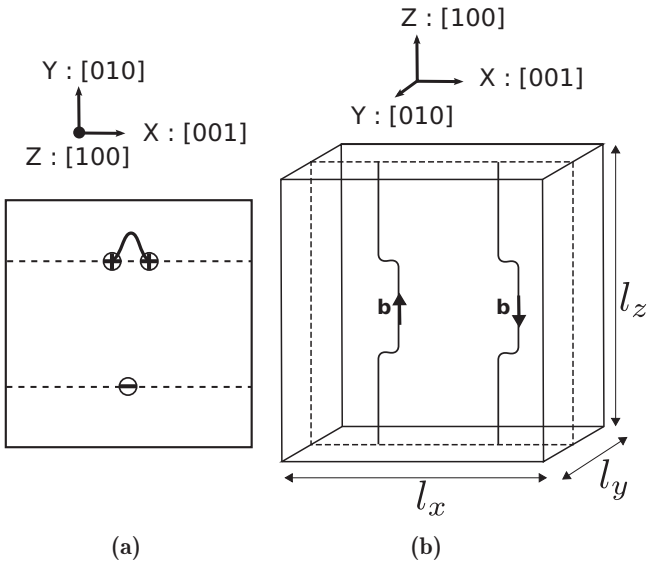

FIG. 2. Schematic view of the simulation cells. (a) 2D system used for NEB calculations of Peierls potential. Points (−) and (+) represent the two opposite screw dislocations of the dipole axis normal to the (010) glide plane (marked as a dotted line). As sketched out, NEB calculations are performed between two equivalent positions of dislocation (+) (see text for details). (b) 3D system containing a dipole of kinked dislocations aligned in (010) glide plane. The system is built so that periodic kinks are distant from $l_z/2$.

in this case; the periodicity along the dislocation line is broken by the presence of kinks.

A. Peierls potential calculation

The 2D system is built so that two dislocations of opposite Burgers vectors ±[100] lie along the Cartesian Z direction [Fig. 2(a)]. The glide plane (010) is normal to the Y direction. To ensure the periodicity of the system along the X direction, a tilt component equal to $b/2$ is applied to the Z axis [41]. The NEB method, as implemented in LAMMPS [42–44], is used to calculate the minimum energy path (MEP) of one dislocation displaced along X from an initial stable configuration to the next stable configuration. The initial and final positions of the dislocation (+) are shifted by ±[100]/2 along X with respect to the dislocation (−) coordinate (i.e., the dipole axis). Initial and final configurations along the MEP are therefore symmetrical with respect to the dipole axis. The MEP is sampled using 24 images, bonded with a spring constant of 0.1 eV/Å. The initial and final configurations are generated by applying the isotropic displacement field of a screw dislocation to the atomic coordinates, and then relaxed. The intermediate configurations are linearly interpolated from the initial and final states. We use a force convergence criterion of 0.01 eV/Å to minimize the states string.

NEB calculations are first performed using a constant-volume approach (with initial cell lengths scaled on the equilibrium lattice parameters of bulk Mg-Pv at 30 GPa of pressure) so only internal energy E is of concern in the MEP [45]. In order to minimize the fluctuations of the hydrostatic pressure along the MEP, the system size is increased to 152 Å × 215 Å × b. Once the MEP is determined, all images

are also rescaled according to the equation of state of Mg-Pv [38] to compute the MEP in a constant-pressure approach. Consistently with the use of a large supercell system, we further verify that a constant-pressure approach leads to the same MEP in which enthalpy H is now of concern.

Because the calculation involves a dipole configuration embedded with periodic boundary conditions, periodic image effects have to be taken into consideration [41,46–48]. Thus, the contribution of elastic interaction of dislocations is subtracted from MEP, using anisotropic elasticity theory [49,50]. This term typically amounts to less than 0.03 eV/b within our system size.

B. Kink-pair calculation

The determination of formation enthalpy of a kink pair requires a 3D simulation system, in which a kink pair can be developed along the dislocation line. We use thus a setup where the dislocation dipole is aligned in the glide plane, i.e., dislocation lines are along the Z direction and equally spaced along X, as illustrated in Fig. 2(b). Moreover, the system is built to ensure that the width between kinks belonging to the same line is equal to half the length l_z of the dislocation line. Dimensions l_x and l_y are larger than l_z in order to minimize the elastic interactions between kinks of opposite lines. Without applied stress, a kink pair of finite width should be unstable. However, the use of periodic boundary conditions along the kinked lines allows one to stabilize well developed kink pairs localized every $l_z/2$. Initial sharp nonrelaxed kinks are introduced in the system by gathering straight dislocation lines of length $l_z/2$. The kinked dipole system is then minimized and kink enthalpy H_k is obtained from the difference between the kinked system and straight dipole. As for NEB calculations, we ensure that both constant-volume and constant-pressure approaches lead to similar results.

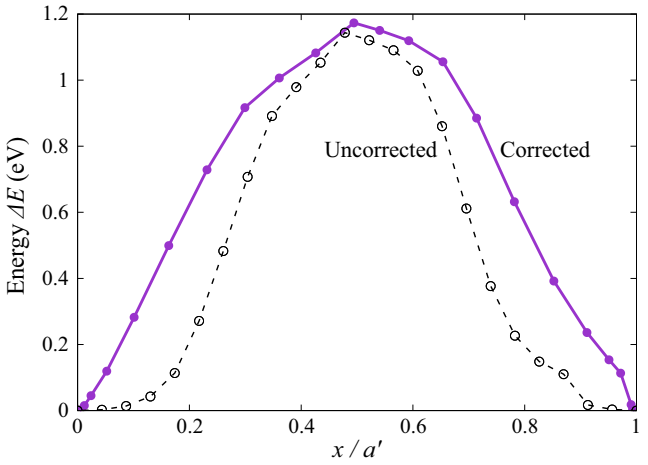

FIG. 3. MEP associated with the glide of a straight screw dislocation line (length b) of Burgers vector [100] in (010) at a pressure of 30 GPa. Open symbols correspond to ΔE plotted with respect to a linearly interpolated reaction coordinate. The Peierls potential V_p (taking the elastic dipole interactions into account) plotted as a function of the reduced dislocation position x_c/a' is shown as filled symbols.

III. RESULTS

A. Peierls potential

The energy barrier that the dislocation has to overcome, resulting from NEB calculation, is shown in Fig. 3. In Fig. 3, the MEP is plotted as a function of the linearly interpolated coordinate and also as a function of the dislocation position. To serve as reaction coordinate, the dislocation position has been determined for each of the 24 images according to the following procedure: for each image, we extract from the atomistic configuration the disregistry $\phi(x)$ in the glide plane (Fig. 4). All disregistries are then fitted according to the following equation:

$$\phi(x) = \frac{b}{2} + \frac{b_1}{\pi}\arctan\left(\frac{x-x_1}{\zeta_1}\right) - \frac{b_2}{\pi}\arctan\left(\frac{x-x_2}{\zeta_2}\right),$$

where b_i, x_i, and ζ_i are adjustable parameters. The only restriction is on b_i, for which $b_1 + b_2$ has to be equal to the magnitude of the Burgers vector b. The reaction coordinates is then defined by the coordinate of the dislocation center $x_c = \frac{b_1 x_1 + b_2 x_2}{b}$.

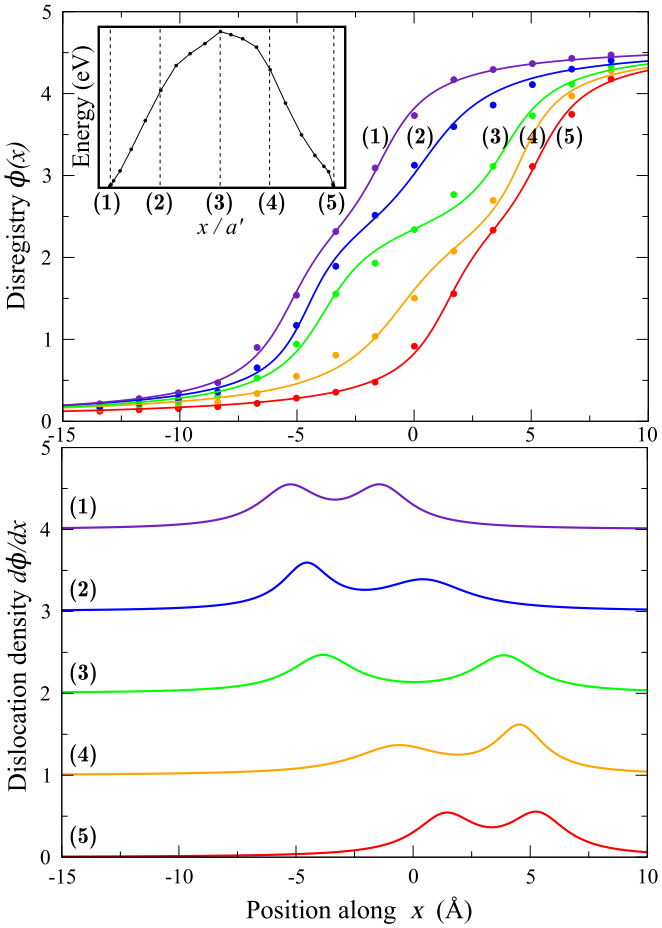

FIG. 4. Atomic screw disregistries $\phi(x)$ (top panel) and Burgers vector densities $\frac{d\phi(x)}{dx}$ (bottom panel) plotted as a function of the distance to the core center in (010). The five core configurations correspond to the positions of the dislocation along the MEP shown in the inset. Disregistry functions $\phi(x)$ are computed according to Mg and Si sublattices.

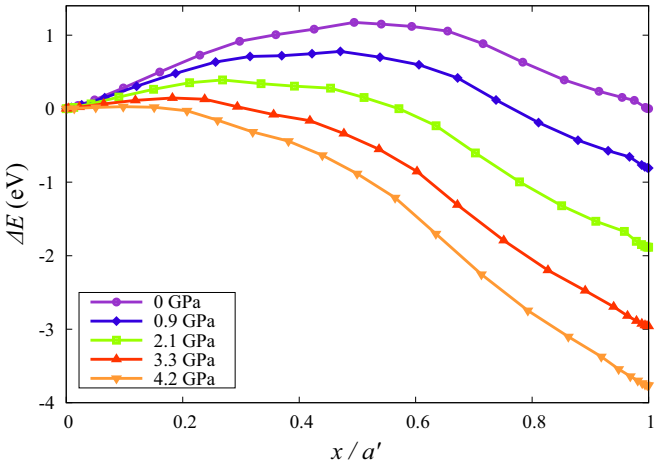

FIG. 5. Minimum energy path ΔE for a straight screw dislocation of line length b plotted as a function of an applied stress ranging from 0 to 4.2 GPa.

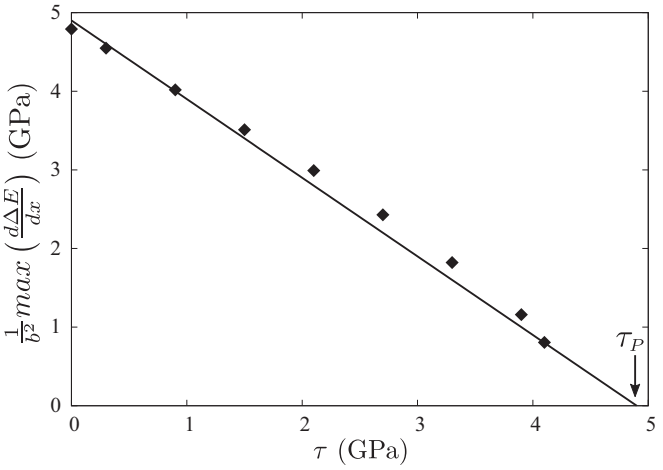

FIG. 6. Critical stress required to overcome the Peierls potential as a function of applied stress τ. These critical stresses are taken as the maximum of the derivative of ΔE.

Once ΔE has been corrected of the dislocation position along the MEP and the elastic dipole interactions, the resulting barrier (continuous thick line in Fig. 3) corresponds to the Peierls potential V_p felt by the dislocation under zero stress. We further check that the dipole configuration investigated here does not lead to system size effect on V_p. Indeed, compared to a 114 Å × 161 Å × b system, the Peierls potential extracted from a 152 Å × 215 Å × b configuration changes by less than 0.02 eV/b. V_p appears thus to be asymmetric with respect to the dislocation position with a maximum of 1.17 eV/b at halfway of the path.

Figure 4 shows the evolution of the dislocation core structure as it crosses the energy barrier. It can be seen that the dislocation does not move as a whole but rather evolves through the displacement of fractional dislocations. Following Refs. [34,40], we use the terminology fractional because the stable core configuration, although compact, is associated with a Burgers vector density displaying two peaks in (010) [see core configuration (1) or (5) on Fig. 4]. When the dislocation stays out of its equilibrium position, the fractionals are decoupled as illustrated by the Burgers vector density (2) or (4). At the saddle point of ΔE, the Burgers vector density shows a clear dissociation of the dislocation core, with two fractional dislocations located exactly in the two adjacent Peierls valleys.

To further analyze the possible dependence of the Peierls potential with respect to an applied shear stress, we also perform NEB calculations using the same setup on which we add a fixed strain component ε_{yz} (Fig. 5). We apply positive or negative strain ε_{yz} to promote glide along either [001] or [00$\bar{1}$]. Practically, it means starting either from the core configuration (1) (Fig. 4) and applying $\varepsilon_{yz} > 0$ or from core (5) (Fig. 4) and applying $\varepsilon_{yz} < 0$. It turns out that whatever the sign of the applied strain, the dislocation glide always involves climbing the potential along the highest slope (i.e., the left side slope of Fig. 3). Extracting the maximum slope of ΔE (Fig. 5) and plotting it as a function of the applied stress, we find a linear relationship between the two quantities (Fig. 6) suggesting that the Peierls stress τ_P should not strongly depend on the applied stress. This is further verified by isolating V_P from ΔE using the relationship $\Delta E = V_P + a'b\tau$. The evolutions of V_p as a function of the various applied stresses are shown in Fig. 7. One can notice that V_P is stress dependent and always asymmetric. Indeed, the maximum of V_P changes by 0.2 eV/b. However, as evidenced in Fig. 6, whatever the applied stress, the Peierls stress (scaling on the highest slope of V_P) remains rather constant. From Fig. 6, one can estimate a Peierls stress τ_P of 4.9 GPa according to the scaling of the maximum of $d\Delta E/dx$ with $\tau_P - \tau$.

B. Kink-pair nucleation enthalpy

Knowing the Peierls potential, now we compute the critical kink-pair nucleation enthalpy ΔH_k^* using the elastic interaction model [12,17]. In our formulation, the shape of the bow out of the kink-pair mechanism is prescribed to be trapezoidal (Fig. 8). Therefore, the bow out will be described by three

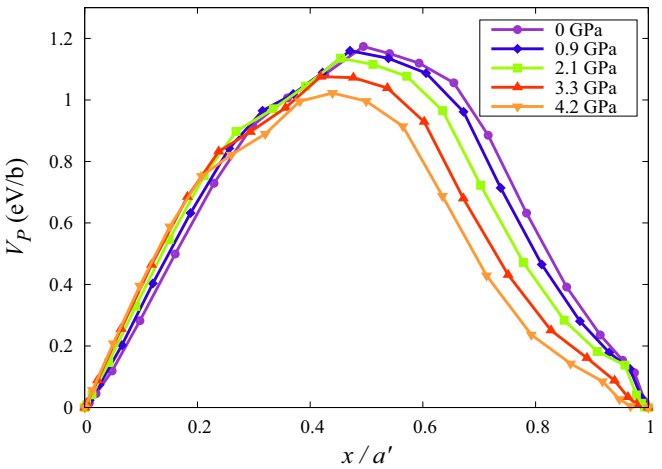

FIG. 7. Evolution of the Peierls potential $V_P(x)$ felt by the screw dislocation of Burgers vector [100] as a function of applied stress. As explained in the text, V_P is extracted from the evolution of ΔE after removing the work of the applied stress τ. It is interesting to note that the Peierls stress τ_P appears rather insensitive to τ.

geometrical parameters: a kink-pair height h, a projected kink length l, and a separation distance between kinks w. As demonstrated in Ref. [51], the trapezoidal description leads to a kink-pair geometry consistent with line tension description and has the advantage that the elastic energy difference $\Delta E_{\rm elas}$ between the bow-out configuration and the straight dislocation can be written using the elastic energy formula of each piecewise straight planar dislocation [10]. In particular, $\Delta E_{\rm elas}$ [Eq. (1)] involves a change in self-energies $\Delta E_{\rm self}$ of the various segment of the bow out [Eq. (2)] plus a change of the interactions energies $\Delta E_{\rm int}$ [Eq. (3)].

According to Refs. [10,18], $\Delta E_{\rm self}$ and $\Delta E_{\rm int}$ can be written as

$$\Delta E_{\rm self} = \frac{\mu b^2}{4\pi}\left[2\frac{l^2+h^2/(1-\upsilon)}{\sqrt{l^2+h^2}}\ln\left(\frac{\sqrt{l^2+h^2}}{e\rho}\right) + w\,\ln\left(\frac{w}{w+2l}\right) - 2l\,\ln\left(\frac{2l+w}{e\rho}\right)\right] \quad (2)$$

and

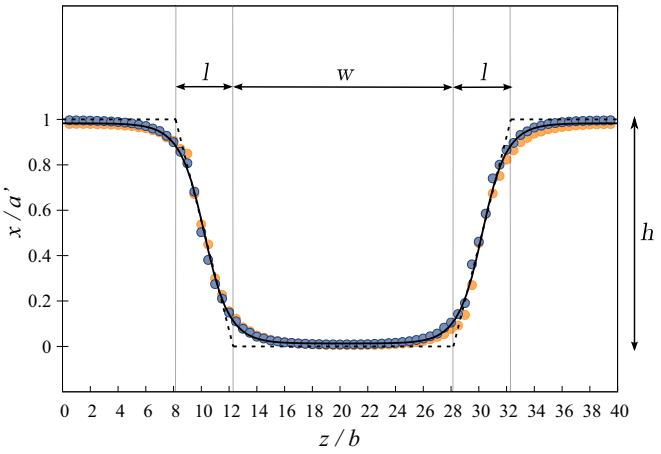

FIG. 8. Kink-pair shape calculated within a periodic supercell of length $40b$. Blue and yellow circles correspond, respectively, to the center location of the positive and negative dislocation disregistries. The solution of the kink-pair model is shown as a dotted line. It is worth noticing that minimizing Eq. (5) with respect to the projected kink length l leads to a kink shape in excellent agreement with the atomistic calculation.

$$\begin{aligned}\Delta E_{\rm int} = \frac{\mu b^2}{2\pi}\Bigg[&\sqrt{h^2+(l+w)^2}-\sqrt{l^2+h^2}-w+(w+2l)\ln\left(\frac{2(w+2l)}{\sqrt{h^2+(l+w)^2}+l+w}\right)\\ &+l\,\ln\left(\frac{\sqrt{h^2+(l+w)^2}+l+w}{\sqrt{l^2+h^2}+l}\right)\Bigg]+\frac{\mu b^2}{4\pi}\frac{1}{l\sqrt{l^2+h^2}}[l^2+h^2/(1-\upsilon)]\Bigg[w\,\ln\left(\frac{\sqrt{h^2+(l+w)^2}+\sqrt{l^2+h^2}}{\sqrt{h^2+(l+w)^2}-\sqrt{l^2+h^2}}\right)\\ &+2(w+l)\ln[\sqrt{l^2+h^2}(l+w)+l\sqrt{h^2+(l+w)^2}]-2(w+l)\ln[(\sqrt{l^2+h^2}+l)]\\ &-2(w+l)\ln[\sqrt{l^2+h^2}+\sqrt{h^2+(l+w)^2}]\Bigg], \end{aligned} \quad (3)$$

where b is the length of the Burgers vector, μ the shear modulus, υ the Poisson's ratio, and ρ a cut-off length controlling the core energies of dislocation segments. In the following, μ and υ are respectively taken as 179 GPa and 0.27 for Mg-Pv at a pressure of 30 GPa [40].

The work done by the applied stress W_τ is simply $\tau bh(l+w)$ and the difference in Peierls energy of the kink pair with respect to the straight line is given by

$$\Delta W_P = 2\frac{\sqrt{l^2+h^2}}{h}\int_{x_0}^{x_0+h} V_P(x)dx + w[V_P(x_0+h) - V_P(x_0)] - 2lV_P(x_0), \quad (4)$$

where x_0 is the equilibrium position of the infinite straight dislocation under an applied stress τ.

The metastable configuration of the kink pair corresponds therefore to a saddle point of ΔH_k [Eq. (1)] with respect to the three parameters h,l,w. Nevertheless, there remains an undefined parameter ρ which does not influence the physics of the nucleation but may have an effect on the absolute critical nucleation enthalpy ΔH_k^*. We thus parametrize the cut-off length ρ based on the atomistic calculation of $2H_k$ for an isolated kink of full height a'. Indeed, in the limit of $\tau \to 0$, the enthalpy of one isolated kink follows [18]:

$$\begin{aligned} 2H_k &= \Delta H_k^*(\tau=0)\\ &= \frac{\mu b^2}{2\pi}\left[\frac{l^2+a'^2/(1-\upsilon)}{\sqrt{l^2+a'^2}}\ln\left(\frac{\sqrt{l^2+a'^2}}{e\rho}\right) - l\,\ln(l/e\rho) + l\,\ln\left(\frac{2l}{l+\sqrt{l^2+a'^2}}\right) + l - \sqrt{l^2+a'^2}\right]\\ &\quad + 2\frac{\sqrt{l^2+a'^2}}{a}\int_0^{a'} V_P(x)dx. \end{aligned} \quad (5)$$

Therefore the cut-off length ρ can be adjusted in such a way that by minimizing the previous equation with respect to l, we match the value $2H_k$ computed atomistically in the following section.

C. Atomistic calculation of isolated full height kinks

Full height a' kinks are calculated using 3D systems of length l_x and l_y increased, respectively, to 423 and 295 Å. Figure 9 shows how the excess enthalpy H evolves as a function of kinked line length l_z. Single isolated kink enthalpy

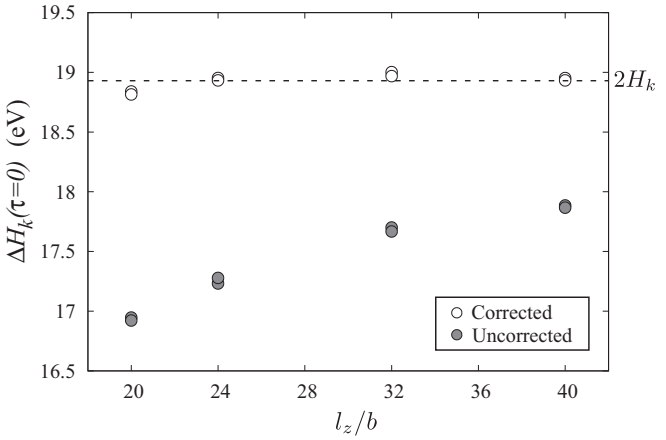

FIG. 9. Convergence of the enthalpy of kinked dislocation dipole with respect to the system size l_z. After applying the relevant elastic correction, $2H_k$ converges to an asymptotic value of 18.90 eV. For each cell length l_z, results are shown for two different system sizes: 315 Å × 219 Å × l_z and 423 Å × 295 Å × l_z.

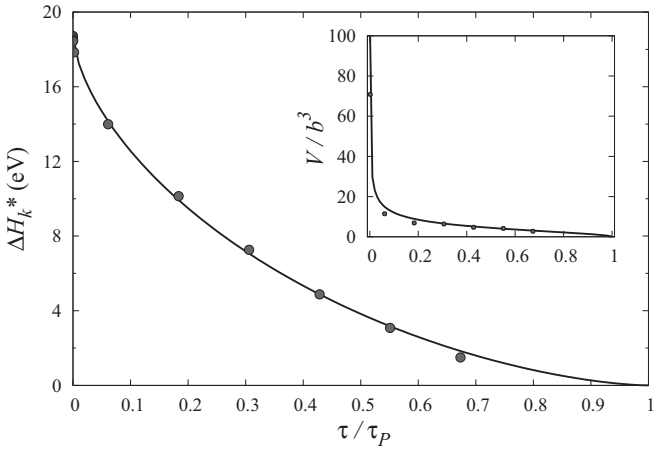

FIG. 10. Saddle-point enthalpy ΔH_k^* as a function of stress τ. The inset panel displays the evolution of the activation volume for the kink-pair nucleation as a function of τ. In both figures, the trend line corresponds to an adjustment of the data with respect to $\Delta H_k^*(\tau) = 2H_k[1-(\tau/\tau_P)^p]^q$ with $p = 0.65$ and $q = 1.56$.

H_k can further be evaluated from Fig. 9 by taking into account the kink-kink interaction $W_{\rm int}$ along the dislocation line.

In the framework of a trapezoidal kink pair, the kink-kink interaction energy $W_{\rm int}^0$ between two oblique kinks separated by w can be evaluated by developing the elastic energy [Eq. (2) + Eq. (3)] of the kink pair to the first power in $1/w$. It follows that $W_{\rm int}^0$ corresponds to a negative kink-kink interaction given by Eq. (6). As expected, $W_{\rm int}^0(w)$ is also a function of the projected kink length l and reduces to the classical expression $-\frac{\mu b^2 a'^2}{8\pi w}\frac{1+\upsilon}{1-\upsilon}$ [10], in the case of an abrupt kink (i.e., $l = 0$).

$$W_{\rm int}^0(w) = \frac{\mu b^2}{4\pi w}\left[\frac{a'^2}{2} + l^2 + \frac{\left(l^2 + \frac{a'^2}{1-\upsilon}\right)\left(\frac{a'^2}{\sqrt{l^2+a'^2}+l} - 2\sqrt{l^2+a'^2} + l\right)}{\sqrt{l^2+a'^2}}\right]. \quad (6)$$

Finally, the integration of the infinite periodicity along the dislocation line l_z leading to $W_{\rm int} = \ln(4)W_{\rm int}^0(l_z/2)$, our atomistic results converge to $2H_k = 18.90$ eV as shown Fig. 9.

Kink shapes can also be analyzed by computing the disregistry in (010) glide plane (Fig. 8). For the largest separation distance investigated here, we check that both kinks are well developed with a projected size l around 20 Å. The kink pair corresponds to two opposite kinks of mixed character close to 20°. Kink lengths or characters do not seem to strongly depend on kink sign, in agreement with the fact that both kinks are widely spread over the Peierls potential.

D. Prediction of the elastic interaction model

The cut-off length ρ appearing in the elastic interaction formulation is parametrized according to the previous results. ρ has to be chosen in such a way that minimizing Eq. (5) according to l leads to a critical configuration of isolated kink which coincides with the results of atomistic calculations. The best agreement is found for a value of $0.2b$. According to the elastic model, the isolated kink shows a projected length $l = 4.11b$ and its critical enthalpy $2H_k$ corresponds to 18.91 eV; both length and energy are thus in quantitative agreement with the atomistic calculations.

For each value of stress τ, we use Eqs. (1)–(4) and rely on the procedure proposed by Ref. [18] to search for the saddle-point configuration h^*,l^*,w^* and the corresponding critical nucleation enthalpy ΔH_k^*. Figure 10 shows the evolution of ΔH_k^* as a function of τ. It is worth noticing that at each stress, the critical nucleation enthalpy is computed with respect to the stress-dependent Peierls potential V_P as shown Fig. 7. As the applied stress increases, ΔH_k^* decreases very rapidly from $2H_k$ down to zero for $\tau = \tau_P$. $\Delta H_k^*(\tau)$ follows the general parametric form proposed by Kocks and co-workers [52]. Regarding the critical kink-pair geometry, we find that the height h^* of the critical bulge decreases continuously with the increasing stress. In the meantime, we observe a strong evolution of both the size of the kinks l^* and their equilibrium width w^*. At $0.1\tau_P$, the kink size l^* is equal to $3b$, while the width is now $w^* = 3b$. We lose the trapezoidal shape around $0.25\tau_P$. Above, the critical bulge corresponds to a shadow triangle (i.e., w^* below b) with kink size reincreasing. In any case, the activation volume $h^*b(w^* + l^*)$ decreases continuously as shown in Fig. 10.

IV. DISCUSSION

A. Asymmetry of the Peierls potential

Generally, an asymmetric Peierls potential is expected on the basis of geometrical considerations resulting from crystal chemistry or lattice. Low symmetry crystals meet such requirement but it could also happen in the case of higher symmetry crystals where different displacements of dislocation involve different rearrangements of atoms as in bcc metals along the twinning or antitwinning directions [53–55]. As Mg-Pv crystallizes in a low symmetry orthorhombic structure, it is not surprising to find an asymmetric Peierls potential (Fig. 3

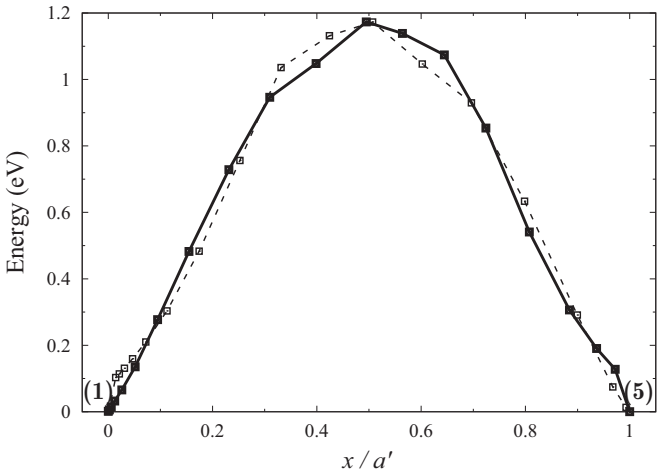

FIG. 11. MEP for dislocation glide along [001] and [00$\bar{1}$]. Whatever the way, paths involve the climb of the highest slope. The two paths reach the same maximum energy, associated to the core configuration (3) in Fig. 4.

or Fig. 7). However, for geometrical considerations, such asymmetry leads necessarily to different Peierls stresses as the dislocation is forced to move along one or opposite direction. Again, one of the best examples of such situation is given by the occurrence of twinning/antitwinning in bcc metals [53–55]. We further show here that, whereas the Peierls potential of [100] screw dislocation in (010) is highly asymmetric, we find a unique Peierls stress τ_P whatever the sign of applied stress. This result confirms recent atomistic calculations [34] showing that the stress level at which a [100](010) screw dislocation core starts to move is insensitive to the sign of the applied stress. There is therefore an apparent discrepancy between an asymmetric potential and a single Peierls stress. The underlying reason is that the asymmetry in the potential is not related to geometrical considerations but that instead, it is linked to the motion of the dislocation itself. For the sake of clarity, let us consider that we apply ε_{yz} to move a dislocation initially located in (1) (Fig. 4) to location (5). NEB calculation based on configurations extracted from the dislocation gliding leads to the Peierls potential (Fig. 3) reported in Fig. 11. From the final state [dislocation in position (5)], applying now $-\varepsilon_{yz}$, the dislocation moves backwards to position (1). During this second step, the computed Peierls potential shown in Fig. 11 is strictly the mirror of the first one with respect to the dislocation path. It means that whatever the sign of the applied stress, we find a single Peierls stress τ_P of 4.9 GPa close to the value reported in Ref. [34] and corresponding to the highest slope of V_P.

The origin of this dynamically asymmetric potential can be related to the gliding process. From the atomistic point of view, the two paths involve indeed different atomic displacements but the same dissociation mechanism.

During the motion of the straight dislocation, we observe in Fig. 4 that the first event corresponds to the motion of the leading fractional dislocation. This first event corresponds to a limited stage during which the system has to provide not only extra energy or enthalpy for the fractional motion but also the necessary energy associated with the increase of unstable stacking fault ribbon. At the end of this step, the trailing fractional moves and closes the stacking fault ribbon extended over one lattice valley. This last process, involving also a fractional displacement, is now helped by the closure of the unstable stacking fault leading thus to the asymmetry. The crossing point of the two MEPs (Fig. 11) corresponds exactly to the maximum value of ΔE and to the dissociated state of the dislocation [position (3) in Fig. 4].

B. Activation enthalpy for kink-pair mechanism

The activation enthalpy for the kink-pair mechanism involves both nucleation and migration of kinks. It is, however, common to find that only one of the two processes acts as a limiting factor. In the case of Mg-Pv, we show that the kinks are widely spread over the Peierls potential. Our calculations show that, without stress, the kink length l is around 20 Å. Under stress, the critical configuration for kink-pair nucleation always involves individual kinks with lengths larger than $3b$ (i.e., 15 Å). Such widely spread kinks should therefore bear low migration enthalpy barrier. This assumption can be verified considering the well-known Frenkel-Kontorova model [56].

The kink-pair shape shown in Fig. 8 can be accurately reproduced by $x/a' = \frac{2}{\pi}\arctan[\exp(\frac{\pi z}{\lambda b})]$ where λ can be viewed as a measurement of the kink size. Here we find $\lambda \approx 4$. As using the Frenkel-Kontorova model, H_k scales with $2/\pi\lambda$ whereas H_m (the migration enthalpy) evolves with $\exp(-\pi\lambda)$, one can easily show that H_m in our case is one order of magnitude lower than H_k. The kink-pair mechanism in Mg-Pv can thus be assumed to be controlled by the nucleation of the kink pair.

C. Implications for the plastic behavior Mg-Pv

Our calculations confirm that Mg-Pv can be considered as a high lattice friction material with $\tau_P/\mu > 2.510^{-2}$. For comparison, at similar high-pressure conditions, the normalized Peierls stress for bcc tantalum [57] never exceeds 10^{-2}. At a pressure of 30 GPa, the Peierls stress $\tau_P = 4.9$ GPa found in this study is consistent with the few available experimental data for Mg-Pv strength under pressure. Indeed, the strength of Mg-Pv is expected to be lower than 10 GPa [3,5], measured in polycrystalline aggregates. One can also note that we agree well with the 5.8 GPa value reported in Ref. [4]. Nevertheless, we show here that the critical stress for plastic flow should strongly depend on temperature as is reflected by the evolution of $\Delta H_k^*(\tau)$. In conjunction with Orowan's equation, one generally assumes that ΔH_k^* scales linearly with kT [29]. We can predict that, for typical laboratory strain rate, the flow stress will drop by about 20% at room temperature.

Following the derivation of line tension model given in Ref. [18], we also verify that the kink enthalpy H_k at zero stress can be approximated by the following equation:

$$H_k = \frac{\mu b^3}{2}\sqrt{\tau_P/\mu}, \tag{7}$$

where H_k only depends on the shear modulus and on the Peierls stress. When dealing with a high lattice friction material under high hydrostatic pressure, it is therefore not surprising to find H_k around 9.45 eV [Eq. (7) approximates H_k to 9.32 eV]. Considering that H_k defines the upper limit of

the temperature range in which Mg-Pv deforms through a kink-pair mechanism, we demonstrate that the Peierls stress remains a useful quantity to characterize deformation mechanisms even at relatively high temperature.

V. CONCLUSION

We develop a numerical scheme to study the glide of [100](010) screw dislocation in Mg-Pv, based on atomistic calculations and an elastic interaction model for kink-pair mechanism. The Peierls potential is shown to be dynamically asymmetric and characterized by a Peierls stress of 4.9 GPa. Atomistic calculations of kink pairs show that kinks are widely spread over the Peierls potential with an enthalpy H_k scaling with the Peierls stress. Our results demonstrate that in this high lattice friction material, the kink-pair mechanism is controlled by the nucleation event of kink pairs.

ACKNOWLEDGMENTS

This work was supported by funding from the European Research Council under the Seventh Framework Programme (FP7), ERC Grant No. 290424—RheoMan. Ph.C. thanks Pr. Koizumi for helpful discussions regarding the implementation of the elastic interaction model.

[1] L.-G. Liu, Phys. Earth Planet. Inter. **11**, 289 (1976).
[2] K. Hirose, J. Geophys. Res. **107**, ECV 3-1 (2002).
[3] C. Meade and R. Jeanloz, Nature **348**, 533 (1990).
[4] J. Chen, D. Weidner, and M. Vaughan, Nature (London) **419**, 824 (2002).
[5] S. Merkel, H. R. Wenk, J. Badro, G. Montagnac, P. Gillet, H.-K. Mao, and R. J. Hemley, Earth Planet. Sci. Lett. **209**, 351 (2003).
[6] P. Cordier, T. Ungár, L. Zsoldos, and G. Tichy, Nature (London) **428**, 837 (2004).
[7] H.-R. Wenk, I. Lonardeli, J. Pehl, J. Devine, V. Prakapenka, G. Shen, and H.-K. Mao, Earth Planet. Sci. Lett. **226**, 507 (2004).
[8] R. Peierls, Proc. Phys. Soc. **52**, 34 (1940).
[9] F. Nabarro, Proc. Phys. Soc. **59**, 256 (1947).
[10] J. Hirth and J. Lothe, *Theory of Dislocations* (Wiley, New York, 1982).
[11] A. Seeger, in *Structure and Diffusion of Kinks in Monoatomic Crystals*, edited by P. Veyssiere, L. Kubin, and J. Castaing, *Dislocations 1984* (CNRS, Paris, 1984), p. 141.
[12] D. Caillard and J. Martin, *Thermally Activated Mechanisms in Crystal Plasticity* (Pergamon, New York, 2003).
[13] V. Celli, M. Kabler, T. Ninomiya, and R. Thomson, Phys. Rev. **131**, 58 (1963).
[14] P. Guyot and J. E. Dorn, Can. J. Phys. **45**, 983 (1967).
[15] T. Suzuki, S. Takeuchi, and H. Yoshinaga, *Dislocation Dynamics and Plasticity*, edited by U. Gonser (Springer, Berlin, Heidelberg, 1991), Vol. 12 .
[16] A. Seeger and P. Schiller, Acta Metall. **10**, 348 (1962).
[17] H. Koizumi, H. O. K. Kirchner, and T. Suzuki, Acta Metall. Mater. **41**, 3483 (1993).
[18] H. Koizumi, H. O. K. Kirchner, and T. Suzuki, Philos. Mag. A **69**, 805 (1994).
[19] Y. Kamimura, K. Edagawa, and S. Takeuchi, Acta Mater. **61**, 294 (2013).
[20] W. Xu and J. A. Moriarty, Comput. Mater. Sci. **9**, 348 (1998).
[21] D. Rodney and L. Proville, Phys. Rev. B **78**, 104115 (2008).
[22] D. Rodney and L. Proville, Phys. Rev. B **79**, 094108 (2009).
[23] L. Proville, D. Rodney, and M.-C. Marinica, Nat. Mater. **11**, 845 (2012).
[24] L. Proville, L. Ventelon, and D. Rodney, Phys. Rev. B **87**, 144106 (2013).
[25] L. Dezerald, L. Proville, L. Ventelon, F. Willaime, and D. Rodney, Phys. Rev. B **91**, 094105 (2015).
[26] R. Gröger and V. Vitek, Acta Mater. **61**, 6362 (2013).
[27] V. V. Bulatov, J. F. Justo, W. Cai, A. S. Argon, T. Lenosky, M. de Koning, and T. Diaz de la Rubia, Philos. Mag. A **81**, 1257 (2001).
[28] L. Pizzagalli, A. Pedersen, A. Arnaldsson, H. Jònsson, and P. Beauchamp, Phys. Rev. B **77**, 064106 (2008).
[29] L. Kubin, *Dislocations, Mesoscale Simulations and Plastic Flow* (Oxford University Press, New York, 2013).
[30] D. Brunner, S. Taeri-baghbadrani, W. Sigle, and M. Rühle, J. Am. Ceram. Soc. **84**, 1161 (2001).
[31] T. E. Mitchell, P. M. Anderson, M. I. Baskes, S. P. Chen, R. G. Hoagland, and A. Misra, Philos. Mag. **83**, 1329 (2003).
[32] W. Sigle, C. Sarbu, D. Brunner, and M. Rühle, Philos. Mag. **86**, 4809 (2006).
[33] D. Ferré, P. Carrez, and P. Cordier, Phys. Earth Planet. Inter. **163**, 283 (2007).
[34] P. Hirel, A. Kraych, P. Carrez, and P. Cordier, Acta Mater. **79**, 117 (2014).
[35] H. Jónsson, G. Mills, and K. W. Jacobsen, in *Classical and Quantum Dynamics in Condensed Phase Simulations*, edited by G. Berne and D. Coker (World Scientific, Singapore, 1998), Chap. 16, p. 385.
[36] J. Poirier, S. Beauchesne, and F. Guyot, *Deformation Mechanisms of Crystals with Perovskite Structure*, (American Geophysical Union, Washington, DC, 2013), p. 119.
[37] S. Plimpton, J. Comput. Phys. **117**, 1 (1995).
[38] A. R. Oganov, J. P. Brodholt, and G. D. Price, Earth Planet. Inter. **122**, 277 (2000).
[39] Y. Chen, A. Chernatynskiy, D. Brown, P. K. Schelling, E. Artacho, and S. Phillpot, Phys. Earth Planet. Inter. **210-211**, 75 (2012).
[40] K. Gouriet, P. Carrez, and P. Cordier, Modell. Simul. Mater. Sci. Eng. **22**, 025020 (2014).
[41] W. Cai, V. Bulatov, J. Chang, J. Li, and S. Yip, Philos. Mag. **83**, 539 (2003).
[42] G. Henkelman, B. P. Uberuaga, and H. Jónsson, J. Chem. Phys. **113**, 9901 (2000).
[43] G. Henkelman and H. Jónsson, J. Chem. Phys. **113**, 9978 (2000).
[44] A. Nakano, Comput. Phys. Commun. **178**, 280 (2008).
[45] B. B. Karki and G. Khanduja, Am. Mineral. **91**, 511 (2006).
[46] W. Cai, V. Bulatov, J. Chang, J. Li, and S. Yip, Phys. Rev. Lett. **86**, 5727 (2001).

[47] E. Clouet, L. Ventelon, and F. Willaime, Phys. Rev. Lett. **102**, 055502 (2009).
[48] S. Yadav, R. Ramprasad, A. Misra, and X.-Y. Liu, Acta Mater. **74**, 268 (2014).
[49] J. P. Hirth and J. Lothe, J. Appl. Phys. **44**, 1029 (1973).
[50] E. Clouet, Phys. Rev. B **84**, 224111 (2011).
[51] T. Suzuki, H. Koizumi, and H. O. K. Kirchner, Acta Metall. Mater. **43**, 2177 (1995).
[52] U. Kocks, A. S. Argon, and M. Ashby, *Thermodynamics and Kinetics of Slip* (Pergamon, New York, 1975).
[53] K. Edagawa, T. Suzuki, and S. Takeuchi, Phys. Rev. B **55**, 6180 (1997).
[54] R. Gröger, A. G. Bailey, and V. Vitek, Acta Mater. **56**, 5401 (2008).
[55] S. Queyreau, J. Marian, M. R. Gilbert, and B. D. Wirth, Phys. Rev. B **84**, 064106 (2011).
[56] B. Joós and J. Zhou, Philos. Mag. A **81**, 1329 (2001).
[57] L. H. Yang, P. Söderlind, and J. A. Moriarty, Philos. Mag. A **81**, 1355 (2001).